as magnetospheric field lines disconnect from the IMF; or equivalently, the plasma sheet along the dawn and dusk flanks of the oval expands into the polar cap (3). Along the boundary between open and closed field lines a velocity shear exists (say between sunward convection within the oval and antisunward convection further poleward) so that a sun-aligned arc often forms at the interface. However, the arc does not quite extend to the cusp. When the IMF turns southward, rapid merging and convection tailward of magnetic flux resume at the cusp location.

There is ample theoretical (9) and observational evidence (10, 11) to support the conclusion that as flux becomes connected to the IMF, it usually convects around the polar cap circumference at the boundary between open and closed field lines, with the direction of preferred convection being determined by the IMF B_y. The overall motion is antisunward, but the predominant motion is azimuthal. For $B_y > 0$ in the Northern Hemisphere, the direction of convection is toward dawn. Hence the newly opened flux is added to the flanks of the oval inside the existing sun-aligned arc. This gradually leads to the arc becoming separated from the oval and convecting toward higher latitudes. Only after >10 min of southward IMF conditions does the arc become a true θ-aurora: a bifurcation of the polar cap.

This simple model predicts that θ-auroras should appear to move from the dawn side toward the dusk side for $B_y > 0$ in the Northern Hemisphere, and from the dusk side toward the dawn side in the Southern Hemisphere. The one instance in which θ-auroras were imaged in both hemispheres (2) showed precisely this effect. Our model further predicts that if the IMF turns northward again after a θ-aurora is formed, the motion should stop. No data are currently available for investigation of this prediction. The model also implies that long-duration θ-aurora events (several hours) should occur only when the IMF B_z component changes sign every hour or two, as was the case for the long-lived event shown in Fig. 1.

Because of the scheduled launch of the Polar satellite in December 1995, which will include suitable imagers, there soon should be ample opportunity to test our model in detail. The data presented here show that θ-auroras do represent a true isolation of magnetotail plasma in the polar cap (12) and that they are formed only when the IMF turns southward after an extended period of northward conditions.

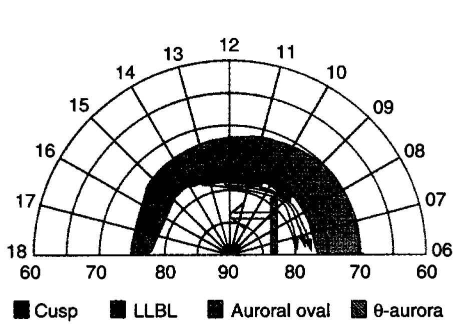

Fig. 5. A simple model illustrating the formation of a θ-aurora. Under northward IMF conditions, polar cap arcs form at the interface between open and closed field lines, but these arcs do not connect up to the polar cusp. When the IMF turns southward and flux is transferred from the dayside to the nightside, the flux is convected along the polar cap boundary and is added to the flanks of the oval inside the arc, pushing the latter to higher latitudes. LLBL, low-latitude boundary layer.

REFERENCES AND NOTES

1. L. A. Frank *et al.*, *J. Geophys. Res.* **91**, 3177 (1986).
2. J. D. Craven *et al.*, *Geophys. Res. Lett.* **18**, 2297 (1991).
3. C.-I. Meng, *ibid.* **8**, 273 (1981).
4. S. Ismail and C.-I. Meng, *Planet. Space Sci.* **30**, 319 (1982).
5. E. W. Hones *et al.*, *Geophys. Res. Lett.* **16**, 37 (1989).
6. J. K. Hargreaves, *The Solar-Terrestrial Environment*, (Cambridge Univ. Press, Cambridge, 1992).
7. The history of the Polar BEAR satellite includes 25 years spent hanging from the ceiling of the Smithsonian Air and Space Museum before being reclaimed and refurbished for launch. More detail can be found in the special issue of the *Johns Hopkins APL Technical Digest* devoted to Polar BEAR (**8**, issue 3, 1987).
8. D. A. Hardy, *Rep. AFGL-TR-84-0317* (Air Force Geophysics Laboratory, Hanscom Air Force Base, Boston, MA, 1984).
9. D. J. Southwood, *J. Geophys. Res.* **92**, 3207 (1987).
10. R. A. Heelis, *ibid.* **89**, 2873 (1984).
11. J. P. Heppner and N. C. Maynard, *ibid.* **92**, 4467 (1987).
12. J. M. Weygand *et al.* (unpublished manuscript) have used the Viking UV imager and automated identifications from the DMSP database to conclude that some polar cap arcs are surrounded by open field lines (polar rain).
13. Supported by NSF grant ATM-9322435 to the Johns Hopkins University Applied Physics Laboratory. D. Hardy and colleagues designed and built the DMSP particle detectors and were generous in sharing data. R. E. Huffman was principal investigator on the Polar BEAR UV imager.

4 May 1995; accepted 6 September 1995

Fission Track Evidence on the Initial Rifting of the Red Sea: Two Pulses, No Propagation

Gomaa I. Omar and Michael S. Steckler

Fission track analyses indicate that the Red Sea initially opened simultaneously along its entire length. Two distinct pulses of uplift and erosion characterized the early stages of rifting in the Red Sea throughout Egypt and in southwestern Saudi Arabia. The first pulse began at ~34 million years ago (Ma). The second pulse began in the early Miocene (21 to 25 Ma) and marked the start of the main phase of extension. These data support a rigid plate model for continental extension. These results also indicate that the initiation of rift flank uplift, and therefore rifting, and volcanism occurred nearly simultaneously. This conflicts with classical models of active and passive extension that predict sequential development of these features.

The Red Sea, with the Gulf of Aden, is the only young example of the splitting of a continent to create a new ocean basin. At present the mode of extension in the Red Sea varies from well-established oceanic accretion in the south to late stage continental rifting in the north (1, 2) (Fig. 1). The along-strike contrasts in the Red Sea provide evidence for south to north propagation for the initiation of sea floor spreading (3, 4).

It is not known, however, whether the initiation of rifting underwent a similar south to north progression. Rigid plate kinematics requires that motion begins simultaneously over the entire length of the Red Sea (Fig. 2). The resulting initiation of a rift valley, and later changes in the opening rate, would occur virtually simultaneously along the length of the Red Sea. In contrast, if the opening of the Red Sea initialized as an unzipping from south to north (Fig. 2), then internal deformation of the plate is required. How well continental breakup is approximated by rigid plate tectonics can be evaluated by examining whether the initiation of continental rifting was synchronous or propagated.

Apatite fission track (FT) analysis has proved to be a powerful tool in studying the timing, magnitude, and geometry of uplift and erosion events of the Red Sea rift flanks (5–8). In the Gulf of Suez, FT analyses of apatites from Precambrian crystalline rocks along its western margin have established that large-scale erosion of the uplifted rift flank began at 21 ± 2 Ma, coeval with the

G. I. Omar, Geology Department, University of Pennsylvania, 240 South 33rd Street, Philadelphia, PA 19104, USA.
M. S. Steckler, Lamont-Doherty Earth Observatory, Palisades, NY 10964, USA.

beginning of the main phase of basin subsidence and extension (*7*). The rapid, rift flank uplift and cooling recorded by the basement rocks indicate that there was a flexural isostatic response to the extension (*9–11*). This rapid, mechanically induced uplift makes the timing of erosion and cooling of the rift flank, as recorded by FT data, an excellent proxy for the timing of large-scale, rapid extension.

We conducted an apatite FT study to determine the timing of rift-related basement uplifts flanking the Red Sea margins to distinguish between the synchroneity or propagation of rifting and the implications for the rigidity of continental plates. In addition, FT analyses help reveal the sequential timing of large-scale extension, volcanism, and uplift along the Red Sea, which has implications for the rift dynamics.

Apatite FT ages obtained in this study fall in the range of 22 to 237 Ma (*12*). Generally, young ages and long mean track lengths (13 to 14 μm) are concentrated within ~100 km from the Red Sea coast and progressively increase and decrease inland, respectively (Fig. 3). This pattern indicates that FT data reflect rift-related uplift and erosion increasing toward the coast. Our data define an overall boomerang-shaped trend on an age-length plot (Fig. 4), which indicates recent exhumation of the basement rocks. Furthermore, the apatite samples from less than 110 Ma (Fig. 4, left) fall on two distinct trends. Both of these trends show a negative correlation between age and mean length, which indicates that there is cooling from levels within the total annealing zone (TAZ; >120°C) and the lower part of the partial annealing zone (~90° to 120°C). Track length distributions at the upper end of each trend are unimodal, narrow, and negatively skewed. The longest mean lengths are >14.5 μm for the older trend and 14.03 μm for the younger trend (Fig. 4). These long mean track lengths with narrow (standard deviations <1.1 μm) distributions indicate rapid cooling from the TAZ and that the age of these samples closely approximates the timing of erosional exhumation. The older trend attests to commencement of an erosion event at ~34 Ma (earliest Oligocene), and the younger trend indicates renewed or increased erosion at ~25 Ma (earliest Miocene). A third, poorly defined trend is also noticeable to the right of the Oligocene trend. The youngest sample on this trend possesses length characteristics similar to those of the other two trends. Its mean track length of 13.89 μm and age of 61 Ma indicate exhumation during Late Cretaceous–early Paleocene time.

The rapid exhumation of basement rocks indicated by our FT data from the Red Sea rift flank in southern Egypt requires sufficient relief at the rift to drive rapid erosion. This relief may result from extension-producing, fault-bounded subsidence within the rift and uplift of the rift flanks or uplift of the rift flanks alone. In the Gulf of Suez region, however, the basin lies near sea level before and after initial rifting, indicating that the relief was generated by uplift of the rift flanks (*13, 14*). Distinct events in FT data are formed because the erosion rate is greatest at the start of a tectonic event as the surface morphology adjusts to the new conditions (*15*). Therefore, the two FT trends represent the beginning of two major uplift and erosion events. The older trend

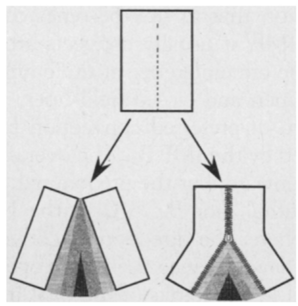

Fig. 2. Two kinematic possibilities for continent breakup. The diagram on the left shows the continental fragments acting as rigid plates. Deformation is limited to the rift zone, which initiates simultaneously along the length of the plate boundary. Changes in the mechanism of extension (continental rifting versus oceanic accretion) can still propagate. The diagram on the right shows the rifting initiating in a limited segment of the future plate boundary and propagating along its length. This "unzipping" necessitates internal deformation of the plate as a result of the differential motion between rifted and intact regions.

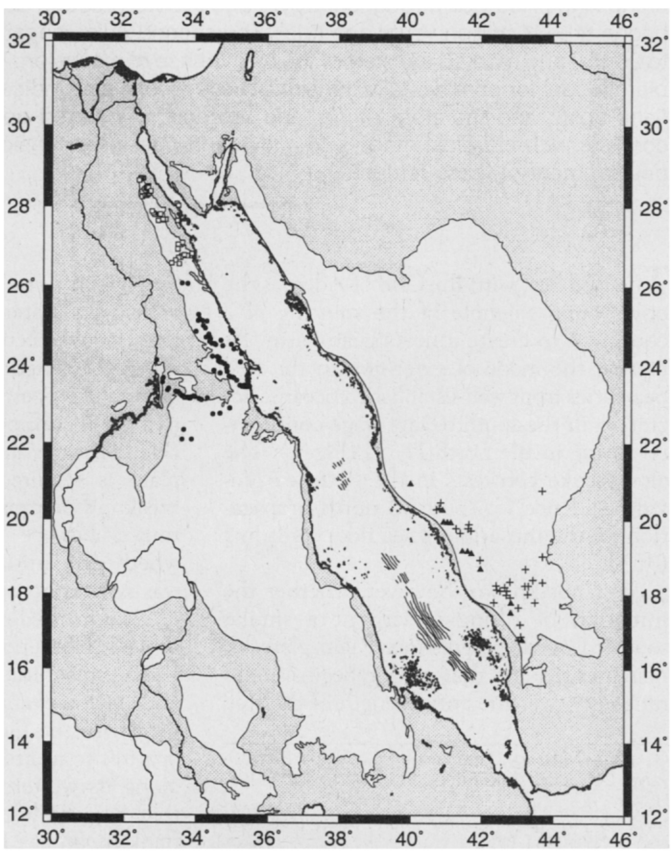

Fig. 1. Map of Red Sea showing locations of the FT samples used here. The basement outcrop flanking the Red Sea is shown in white, and the Phanerozoic sedimentary and volcanic cover are gray. The sample symbols are as follows: closed circles, new Egyptian samples; open squares, Gulf of Suez samples (*7*); plus sign, Saudi Arabian samples (*8*); closed triangles, Saudi Arabian samples on which we made track length measurements. Magnetic anomaly isochrons in the Red Sea (*34*) are indicated by thin lines.

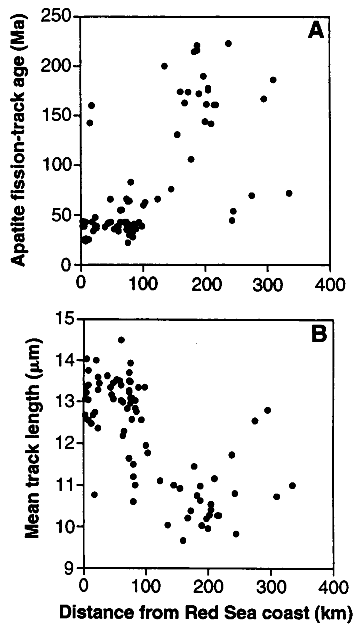

Fig. 3. Relation between FT age (**A**) and mean track length (**B**) as a function of distance from the Red Sea coast.

clearly indicates that large-scale extension dates to the early Oligocene.

Omar *et al.* (*7*) examined FT data from the Gulf of Suez rift flank (Fig. 1) and concluded that rapid extension and basement exhumation began at 21 ± 2 Ma. Furthermore, Steckler and Omar (*16*) showed that a subset of this data from a limited area indicates early Oligocene uplift and erosion. The younger FT ages from the Gulf of Suez and Red Sea portion of Egypt (Fig. 5) suggest that the Red Sea margin in Egypt and the western margin of the Gulf of Suez had experienced the same two-stage exhumation history in the early Oligocene (~34 Ma) and early Miocene (21 to 25 Ma).

To determine if the timing seen in the data from Egypt is maintained throughout the Red Sea, we determined track lengths on 12 additional samples from southwestern Saudi Arabia. These samples were collected from between 17°N and 21°N along the Red Sea margin as part of the FT study described in (*8*). Bohannon *et al.* found that the samples seaward of the erosional escarpment fell along two linear trends on a plot of age versus elevation (Fig. 5, inset), a pattern that results from differential erosion of uplifted blocks. However, they (*8*) were unable to determine the timing of the events that created these two trends. Track length measurements performed on 12 of these samples show a one-to-one correspondence of the age-elevation groupings to the two unroofing trends identified in Egypt (Fig. 5). We conclude that there were two distinct periods of uplift and erosion during the early Oligocene (~34 Ma) and early Miocene (21 to 25 Ma) in the southern Red Sea as well and that these rift events occurred approximately simultaneously throughout the rift. These results strongly support a model of rigid plate kinematics for the early opening of the Red Sea.

Rifting in the Red Sea began at ~34 Ma. This exhumation event indicated by our FT data requires relief at the margin of the Red Sea that could only have been created by extension. The long track lengths of some of the Egyptian samples indicate that uplift and erosion were rapid. This improves the estimates from the early rift sedimentary sections along the Red Sea, which poorly record the beginning of this event. Basal sedimentary units are generally nonmarine, unfossiliferous, and poorly dated. Ages of these strata are estimated as Oligocene on the basis of overlying units or volcanic rocks (*17–20*). Only in the Midyan region of northwest Saudi Arabia do upper Oligocene marine carbonates attest to the beginning of rifting in the early Oligocene (*21*). The earliest volcanic activity also occurred at this time (30 to 33 Ma) (*22–25*). Most of this early volcanism is concentrated to the south, near the Afar hot spot (*25*), whose presence facilitates the melting and volcanism at the start of extension.

Pre-Miocene extension in the Red Sea region is relatively small (*14, 25–27*). The rift flank uplift associated with it is limited to a few hundred meters in the Gulf of Suez and likely increases southward. After this period of relatively slow extension, the FT data clearly show a second period of rapid unroofing in the early Miocene. The southern Egypt data show this transition at ~25 Ma, whereas the Gulf of Suez data indicate 21 ± 2 Ma. However, the age of the Saudi sample with the longest track length is intermediate between these two. Thus, there is no systematic trend in the timing of this event. Our best estimate is 21 to 25 Ma.

Richardson and Arthur (*28*) and Steckler *et al.* (*14*) reported that extension and subsidence rates in the Gulf of Suez basin increased sharply during this unroofing event. Tectonism onshore in southwest Saudi Arabia peaked at ~25 Ma and stopped by 20 to 23 Ma (*8, 20, 29*). An open marine basin developed along the Gulf of Suez and Red Sea at this time (*30*). The frequency of published K-Ar ages on volcanic rocks shows a peak at 20 to 22 Ma (*24, 31*). The style of intrusion also changed at this time (*18, 22, 32*). We interpret this period as the start of the main Red Sea rift phase with faster extension, increased rate of uplift and erosion on the rift flanks, and a focusing of subsidence and volcanism toward the future rift axis.

The sequential timing of extension and rift flank uplift, igneous activity, and regional uplift (doming) may define the mechanisms responsible for continental rifting (*33*). Our data imply that unroofing began during the Oligocene at ~34 Ma; thus, an escarpment had to be created by rifting. The initiation of rifting, uplift and erosion, and volcanism occurred nearly simultaneously along the entire length of the Red Sea. This view conflicts with classical models of active and passive extension that predict sequential development of these features. Any model of the Red Sea and continental rifting in general must be able to account for these observations. One possible model is passive extension of the Red Sea in the presence of a preexisting plume at the Afar hot spot. Lithospheric thinning from the extension would produce upwelling and decompression melting of the anomalously hot asthenosphere, leading to near synchroneity of rifting (and consequently rift flank uplift) and volcanism.

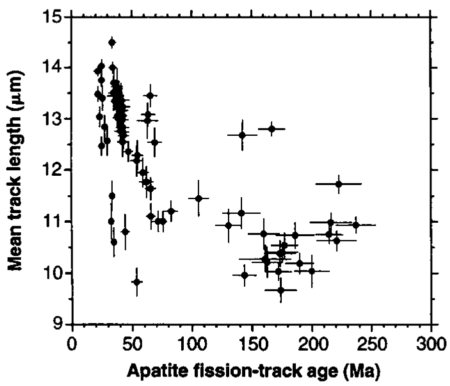

Fig. 4. Plot of mean track length versus FT ages for Red Sea samples. The samples on the left exhibit two distinct trends that indicate exhumation beginning at ~34 Ma and ~25 Ma associated with the opening of the Red Sea. Error bars on the samples correspond to ±1σ.

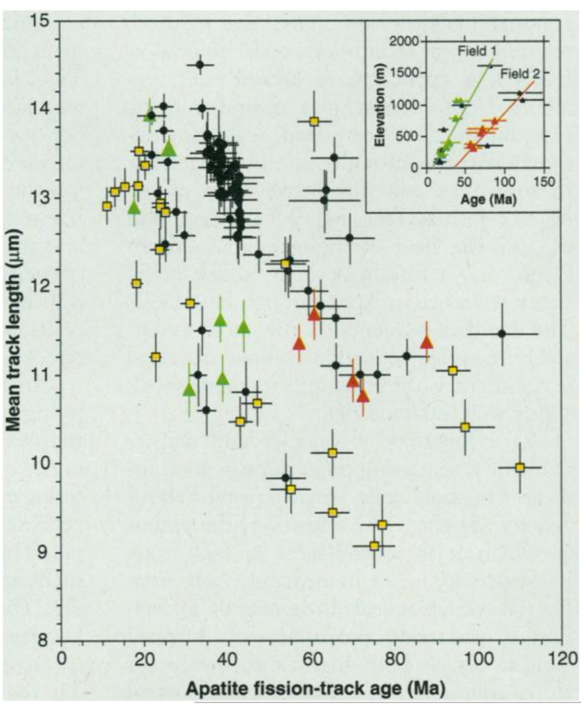

Fig. 5. Close-up plot of the younger part of the FT age (less than 110 Ma; see Fig. 4) versus mean track length for samples from Egypt (symbols as in Fig. 1). The Oligocene cooling trend is dominated by Red Sea samples. The Miocene cooling trend is composed of both Red Sea and Gulf of Suez samples. Samples from southwestern Saudi Arabia (*8*) are indicated by green and red triangles that correspond to fields 1 and 2, respectively, of Bohannon *et al.* (*8*) (inset).

REFERENCES AND NOTES

1. J. R. Cochran, *Am. Assoc. Pet. Geol. Bull.* **67**, 41 (1983).
2. ______, J.-M. Gaulier, X. LePichon, *Tectonics* **10**, 1018 (1992).
3. V. Courtillot, *ibid.* **1**, 239 (1982).
4. E. Bonatti, *Nature* **316**, 33 (1985).
5. B. P. Kohn and M. Eyal, *Earth Planet. Sci. Lett.* **52**, 129 (1981).
6. G. I. Omar, B. P. Kohn, T. M. Lutz, H. Faul, *ibid.* **83**, 94 (1987).
7. G. I. Omar, M. S. Steckler, W. R. Buck, B. P. Kohn, *ibid.* **94**, 316 (1989).
8. R. G. Bohannon, C. W. Naeser, D. L. Schmidt, R. A. Zimmermann, *J. Geophys. Res.* **94**, 1683 (1989).
9. J. Braun and C. Beaumont, *Geology* **17**, 760 (1989).
10. J. K. Weissel and G. D. Karner, *J. Geophys. Res.* **94**, 13919 (1989).
11. P. van der Beek, S. Cloetingh, P. Andriessen, *Earth Planet. Sci. Lett.* **121**, 417 (1994).
12. Preparation of samples for FT analysis, irradiation, counting, track length measurements, calibration techniques, and error calculations are described in (*7*).
13. Z. Garfunkel, *Tectonophysics* **150**, 33 (1988).
14. M. S. Steckler, F. Berthelot, N. Lyberis, X. LePichon, *ibid.* **153**, 249 (1988).
15. G. R. Willgoose, R. L. Bras, I. Rodriguez-Iturbe, *Water Resour. Res.* **27**, 1685 (1991).
16. M. S. Steckler and G. I. Omar, *J. Geophys. Res.* **99**, 12159 (1994).
17. C. Montenat *et al.*, *Tectonophysics* **153**, 161 (1988).
18. J. S. Pallister, *Geol. Soc. Am. Bull.* **99**, 400 (1987).
19. D. L. Schmidt, D. G. Hadley, G. F. Brown, *U.S. Geol. Surv. Open-File Rep. 83-641* (1983).
20. R. G. Bohannon, *Geology* **14**, 510 (1986).
21. H. J. Bayer, H. Hötzl, A. R. Jado, B. Roscher, W. Voggenreiter, *Tectonophysics* **153**, 137 (1988).
22. R. G. Coleman, R. T. Gregory, G. F. Brown, *U.S. Geol. Surv. Open-File Rep. 83-788* (1983).
23. A. Y. Izzeldin, thesis, University of Louis Pasteur, Strasbourg (1982).
24. V. E. Camp and M. J. Roobol, *J. Geophys. Res.* **97**, 15255 (1992).
25. I. Davison *et al.*, *Geol. Soc. Am. Bull.* **106**, 1474 (1994).
26. R. G. Bohannon and S. Eittreim, *Tectonophysics* **198**, 129 (1991).
27. W. Bosworth, *J. Geol. Soc. London Spec. Pub.* **80**, 75 (1995).
28. M. Richardson and M. A. Arthur, *Mar. Petrol. Geol.* **5**, 247 (1989).
29. R. G. Coleman and A. McGuire, *Tectonophysics* **150**, 77 (1988).
30. R. Carella and N. Scarpa, *Proc. Fourth Arab Petrol. Congr.* (1962).
31. D. C. Almond, *Tectonophysics* **131**, 301 (1986).
32. R. G. Coleman, S. DeBari, Z. Peterman, *ibid.* **204**, 27 (1992).
33. A. M. C. Sengör and K. Burke, *Geophys. Res. Lett.* **5**, 419 (1978).
34. H. A. Roeser, *Geol. Jahrb.* **D13**, 131 (1975).

35. The data table and sample coordinates for the FT analysis are available on request from G.I.O. This work was supported by NSF grants EAR 89-17154 (G.I.O.) and EAR 89-16976 (M.S.S.). A special debt of gratitude is owed to the University of Pennsylvania Research Foundation for providing funds to modernize the fission-track laboratory. We thank R. Bohannon and C. Naeser for providing the apatite fractions from southwestern Saudi Arabia. This is Lamont-Doherty Earth Observatory publication number 5404.

10 July 1995; accepted 21 September 1995

Relation of the 1992 Landers, California, Earthquake Sequence to Seismic Scattering

Justin Revenaugh

Measurements of crustal scattering for the area surrounding the 1992 Landers earthquake sequence obtained from regional array recordings of teleseismic events for the 10-year period before the sequence showed that the slip distribution on faults could be deducible from the preshock elastic structure. Scattering intensity correlated strongly with the distribution of aftershocks and slip of the moment magnitude (M_w) 7.3 Landers main shock, M_w 6.1 Joshua Tree, and M_w 6.2 Big Bear events, which implies that aftershocks and slip are structurally controlled and broadly predictable. Scattering within the fault zones was directional and consistent with variable along-strike alignment of stress-induced cracks.

There is abundant evidence that fault bends and jumps play a major role in producing along-fault slip variability and frequently serve as the nucleation point or termination point of major earthquakes (*1*). Evidence about the importance of fault-zone elastic heterogeneity is also accumulating. Recent high-resolution seismic tomography experiments have revealed that the distributions of aftershocks and main shock slip are associated with high-velocity patches within the fault zone, thus implicating fault zone strength as a primary control on earthquake slip (*2*). However, such surveys usually require rich aftershock sequences as the source array necessary for adequate spatial resolution, and thus long, quiescent segments cannot be sampled. Because it is often these segments that are of greatest societal concern, the need for an alternative mode of imaging is clear.

To this end, I have developed a scheme for estimating the short scale length variability in crustal scattering strength on the basis of regional array recordings of teleseismic events (*3*). Because it does not rely on regional or local seismicity, the method, referred to as Kirchhoff coda migration (KCM), is applicable to locked fault segments. Here I report on a ground-truthing experiment that correlated scattering-derived estimates of fault zone heterogeneity to aftershock and slip distributions of the M_w 6.1 Joshua Tree, M_w 7.3 Landers, and M_w 6.2 Big Bear earthquakes in southern California, a foreshock–main shock–aftershock sequence in April through June 1992. The Landers sequence is the most extensively recorded sequence to have occurred in southern California, and its main shock slip is well modeled (*4*).

As a function of velocity and density variability, scattering potential is a good indicator of short scale length crustal heterogeneity (*5*) (Fig. 1A). However, the extent to which it is an indicator of fault zone heterogeneity is not immediately clear from Fig. 1B, which reveals little overall correlation of scattering potential with mapped fault traces, as both highs and lows occur along fault zones (*6*). Nonetheless, several lines of evidence point to a strong component of fault-induced scattering: (i) The correlation length scale of scattering potential (~8 km) is equal to the length scales of seismicity and active fault density (*7*); by comparison, the length scale of topography is greater by a factor of ~4 (~30 km), which indicates that scattering is sensitive to heterogeneity with dimensions characteristic of faulting, not topography. (ii) Contours of aftershock density are deflected where they meet high scattering gradients and visibly neck at crossings (Fig. 1C), which suggests that transitions between high and low scattering delimit fault segments. (iii) The collinear aftershock zones of the Joshua Tree and Landers events follow a series of scattering highs, Big Bear aftershocks are aligned along a pronounced scattering low, and seismicity as a whole clusters near the scattering extremes. (iv) Short scale length variations in scattering potential along the Joshua Tree, Landers, and Big Bear fault zones are associated with aftershock density (Fig. 2). For example, the correlation coefficient measured within a 12.5-km-wide band tracing the Landers fault zone exceeds 0.8 (*8*). Viewed in this way, the scattering potential and gradient clearly are responding to heterogeneity that directly influences aftershock distribution, but the functional form of the relation is complicated by the reversed sense of correlation for the Big Bear sequence.

An assumption used in KCM is that scattering is isotropic; however, because *P*-wave to *S*-wave scattering is not isotropic (*9*), we must be careful to distinguish estimated scattering potential from local scatterer strength, because the latter may be distinctly anisotropic. The northwest alignment of scattering highs and the northeast alignment of lows in Fig. 1B—dominated by the Joshua Tree–Landers and Big Bear aftershock zones, respectively—suggest directional scattering. To test this suggestion, I subdivided the

Crustal Imaging Laboratory, Earth Sciences Department, University of California, Santa Cruz, CA 95064, USA.